

Dual-Pixel Raindrop Removal

Yizhou Li

yli@ok.sc.e.titech.ac.jp

Yusuke Monno

ymonno@ok.sc.e.titech.ac.jp

Masatoshi Okutomi

mxo@ctrl.titech.ac.jp

Tokyo Institute of Technology,
Tokyo, Japan

Abstract

Removing raindrops in images has been addressed as a significant task for various computer vision applications. In this paper, we propose the first method using a Dual-Pixel (DP) sensor to better address the raindrop removal. Our key observation is that raindrops attached to a glass window yield noticeable disparities in DP's left-half and right-half images, while almost no disparity exists for in-focus backgrounds. Therefore, DP disparities can be utilized for robust raindrop detection. The DP disparities also brings the advantage that the occluded background regions by raindrops are shifted between the left-half and the right-half images. Therefore, fusing the information from the left-half and the right-half images can lead to more accurate background texture recovery. Based on the above motivation, we propose a DP Raindrop Removal Network (DPRRN) consisting of DP raindrop detection and DP fused raindrop removal. To efficiently generate a large amount of training data, we also propose a novel pipeline to add synthetic raindrops to real-world background DP images. Experimental results on synthetic and real-world datasets demonstrate that our DPRRN outperforms existing state-of-the-art methods, especially showing better robustness to real-world situations. Our source code and datasets are available at <http://www.ok.sc.e.titech.ac.jp/res/SIR/>.

1 Introduction

Raindrops are typically attached to a glass window or a windshield and refract the light from the scene similar to a fish-eye lens. Therefore, raindrops in images eliminate the original background textures on raindrop-covered regions, which greatly reduces the image visibility and may disturb many computer vision tasks, e.g., object detection [18], video surveillance [20], and autonomous driving [6]. To avoid these disadvantages, removing raindrops in images has been treated as one of the important low-level vision tasks.

Recently, many deep-learning-based methods have been proposed to address single image deraining, including rain streak removal [8, 16, 17, 29, 34, 35, 38] and raindrop removal [11, 26, 28, 32, 33, 43]. Regarding the raindrop removal, representative methods include raindrop-mask-guided methods [11, 26, 32, 33], an edge-guided method [28], and a Laplacian-pyramid-based method [43], as well as general image restoration frameworks [21, 39, 40] validated to be effective on the raindrop removal. Despite the fact that

these state-of-the-art single image raindrop removal methods achieve good performance on synthetic datasets, they often show degraded and limited performance on real-world data, as experimentally pointed out in the survey paper of [15], because of the domain gap between synthetic training data and real-world data. One inherent challenge of the single image raindrop removal is that raindrop detection and removal highly rely on raindrop appearance (e.g., raindrop textures and shapes) observed in a single image. Therefore, they inevitably fail when there are large appearance gaps of raindrops between the synthetic training data and the real-world data at an application phase.

In this paper, we focus on a Dual-Pixel (DP) sensor to better address the raindrop removal task. A DP sensor has been adopted in some consumer digital cameras (e.g., Canon 5D Mark IV and Canon EOS R5) and smartphones (e.g., Google Pixel series and Samsung Galaxy series), as it can be implemented without significantly increasing the cost. As shown in Fig. 1(a), a DP sensor divides each sensing pixel into two halves with left and right photodiodes, by which two individual images called left-half and right-half images can be captured. The summation of these two images, which we call a combined image, corresponds to the image captured by a regular sensor. As shown in Fig. 1(b), for an in-focus scene point within the Depth-of-Field (DoF), the light rays reach the same pixel. In contrast, for an out-of-focus scene point outside the DoF, the light rays reach different pixels, leading to an intensity shift on the horizontal axis between the left-half and the right-half images, which is called a DP disparity. The studies [8, 9, 25, 36] show that the DP disparity can be modeled as different Point Spread Functions (PSFs) of the left-half and the right-half images as shown in Fig. 1(b), where the left-half and the right-half images can be generated from an all-in-focus image by convolution using different disk blur kernels corresponding to their varied PSFs. Recent studies have also demonstrated that the DP disparity is useful for a wide range of applications, such as defocus deblurring [8, 9, 36], autofocusing [9, 9, 13], depth estimation [9, 25, 24], joint deblurring and depth estimation [24], and reflection removal [24]. However, to the best of our knowledge, there is no existing study that adopts a DP sensor for the raindrop removal. Although some of recent rain streak or raindrop removal studies exploit multi-view observations in a stereo or light-field setup [8, 37, 40], the DP sensor has the advantage that it can capture two perfectly aligned and synchronized images in one shot.

A key observation to motivate us to adopt a DP sensor is that, in practical applications requiring raindrop removal such as autonomous driving, the camera is usually background-focused, while the raindrops which are closer to the camera are out-of-focus. Therefore, as shown in Fig. 1(d), the raindrop regions exhibit noticeable DP disparities while other background regions show almost no DP disparity. This suggests that we can utilize DP disparities, instead of solely depending on the raindrop appearance, to detect raindrop locations. Since the DP disparities for raindrops bring slightly-shifted raindrop positions in the left-half and the right-half images, the non-raindrop-covered visible background textures in those images are also shifted. This suggests that we can exploit this redundancy to better restore the background details by fusing the information from the left-half and the right-half images.

With the above motivation, we propose DP Raindrop Removal Network (DPRRN), which consists of two main parts: DP raindrop detection and DP fused raindrop removal. Firstly, the DP raindrop detection part robustly predicts the raindrop masks on the left-half and the right-half images, according to the DP disparities of raindrops. Then, the DP fused raindrop removal part removes the raindrops with the predicted raindrop masks as guide, where we intermediately remove the raindrops from the left-half and the right-half images, respectively, and then fuse and refine those results to obtain the final raindrop removal result as a combined image, i.e., an image captured by a regular sensor. The networks for both parts are

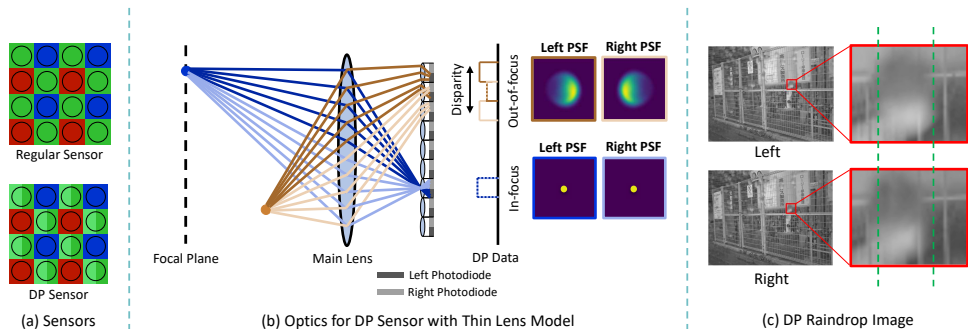


Figure 1: (a) In a DP sensor (Google Pixel 4), each green pixel is split into two halves. (b) The light rays from an in-focus point reach the same pixel, while the light rays from an out-of-focus point reach different pixels in the left-half and the right-half images, producing a DP disparity. The corresponding point spread functions (PSFs), which are used to model the DP disparity, are shown in the right. (c) Raindrops are usually out-of-focus and exhibit DP disparities, while in-focus backgrounds show almost no DP disparity. This motivates us to exploit the DP disparity for raindrop detection and removal.

trained in an end-to-end manner.

Since existing raindrop removal datasets are not applicable to a DP sensor, we built the first DP raindrop removal dataset. To efficiently generate a large amount of training data, we present a novel pipeline to add synthetic raindrops to real-world background DP images. We captured 613 real-world scenes and generated 2,452 pairs of training data with synthetic raindrops. In addition, to test the generalization performance in real-world situations, we also collected a real-world dataset containing 82 DP image pairs with and without real raindrops, which contains raindrop patterns and background textures that are unseen in the training data. Main contributions of this work are summarized as follows:

- We propose the first DP raindrop removal network and dataset. Our network effectively utilizes DP disparities on raindrops for raindrop detection and removal.
- We experimentally demonstrate that our DP raindrop removal network achieves state-of-the-art performance and shows better robustness to real-world situations.

2 DP Raindrop Removal Datasets

2.1 Synthetic-Raindrop Dataset

It is laborious to collect a large number of real-world aligned image pairs with and without real raindrops. It is also hard to accurately simulate DP sensors' inherent characteristics, such as uneven vignetting for the left-half and the right-half images. Therefore, to construct a training dataset for our network, we take a hybrid approach, which only synthesizes raindrops and adds them to real background DP images, which can be easily captured using a real DP camera as usual. In all our experiments, we used Google Pixel 4. Since Google Pixel 4 adopts the DP sensor architecture only to the green pixels, we used green-channel images for our dataset construction, though our dataset construction and network architecture can be easily extended to the RGB color domain.

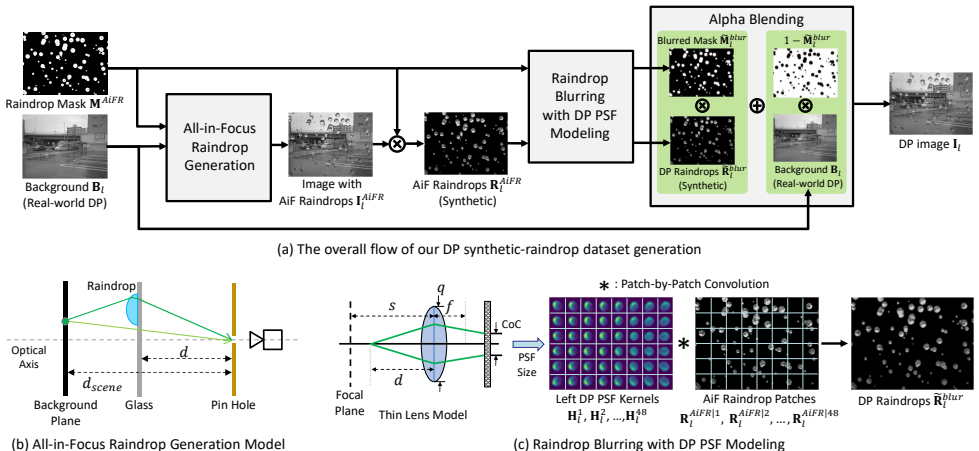


Figure 2: Proposed DP synthetic-raindrop dataset generation: (a) The overall flow for the left-half image, which consists of raindrop generation, raindrop blurring, and alpha blending. (b) A pin-hole model to generate all-in-focus raindrops. (c) The raindrop blurring process with DP PSF modeling. The similar process is conducted for the right-half image.

Figure 2(a) shows the proposed data generation pipeline, where the processes for the left-half image are presented. The processes for the right-half image can similarly be performed. The pipeline consists of three main parts: all-in-focus raindrop generation, raindrop blurring, and alpha blending of synthetic raindrops and a real background.

The first part generates all-in-focus raindrops based on the raindrop refraction model of [10]. For simplicity, as shown in Fig. 2(b), we assume that the whole background has a constant depth d_{scene} and the raindrops (glass) has another smaller constant depth d . We add all-in-focus raindrops to the real-world background DP image \mathbf{B}_l with ray tracing to generate the image with all-in-focus raindrops \mathbf{I}_l^{AiFR} . The locations of the raindrops are determined by a randomly assigned binary raindrop mask \mathbf{M}^{AiFR} , where $\mathbf{M}^{AiFR}(x) = 1$ means that the pixel x is a part of a raindrop region and $\mathbf{M}^{AiFR}(x) = 0$ means that the pixel is in background regions. We set the background depth $d_{scene} = 10m$ and randomly change the raindrop depth d between $15cm$ and $25cm$.

The second part simulates DP disparities for the raindrops. For this purpose, we apply the spatially-varying DP PSF modeling in [56], where in total 6×8 PSF kernel shapes, denoted as \mathbf{H}_l^i for the left-half image, are calibrated for each sub-patch i , as shown in Fig. 2(c). To determine the scale of PSF kernels, we calculated the Circle of Confusion (CoC) radius $r = \frac{q}{2} \times \frac{s'}{s} \times \frac{d-s}{d}$, which corresponds to the PSF radius, where q is the aperture diameter, s' is the distance between the lens and the sensor, s is the focus distance, and d is the assumed raindrop depth. Specifically, using a thin lens model, q is calculated as $q = \frac{f}{F}$ according to Google Pixel 4's focal length f and F-stop F , and s' is calculated as $s' = \frac{fs}{s-f}$, where the focus distance is set as $s = d_{scene}$ because the camera is assumed to be background-focused. According to the calculated CoC radius, we re-scale the PSF kernels to derive \mathbf{H}_l^i in correct PSF size for the real camera.

To blur the all-in-focus raindrops with the above PSF kernels, the raindrops \mathbf{R}_l^{AiFR} are extracted from \mathbf{I}_l^{AiFR} as $\mathbf{R}_l^{AiFR} = \mathbf{M}^{AiFR} \otimes \mathbf{I}_l^{AiFR}$, where \otimes denotes pixel-wise multiplication. Then, the raindrops \mathbf{R}_l^{AiFR} are divided into 6×8 patches and convolved with the PSF kernels

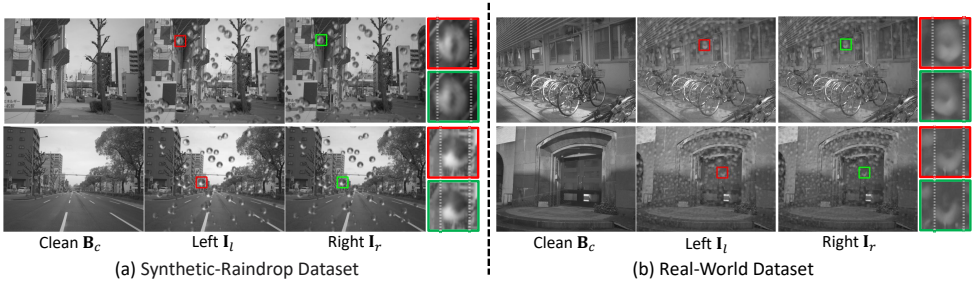


Figure 3: Constructed DP raindrop removal datasets: (a) Synthetic-raindrop dataset, which consists of a real background and synthetic raindrops. (b) Real-world dataset, which consists of both a real background and real raindrops. As depicted in the red and the green boxes, we can successfully simulate the DP disparities on raindrops in our synthetic-raindrop dataset.

in a patch-by-patch manner as $\tilde{\mathbf{R}}_l^{blur|i} = \mathbf{H}_l^i * \mathbf{R}_l^{AiFR|i}$, where $*$ denotes the convolution operation. The sub-patches are then stitched to form the blurred raindrop image $\tilde{\mathbf{R}}_l^{blur}$. Similarly, the binary raindrop mask \mathbf{M}^{AiFR} is also blurred to generate the blurred raindrop mask $\tilde{\mathbf{M}}_l^{blur}$, which is used as the weight for the alpha-blending in the next step.

The final part performs the alpha blending of the synthetic raindrops and the real-world background as $\mathbf{I}_l = \tilde{\mathbf{M}}_l^{blur} \otimes \tilde{\mathbf{R}}_l^{blur} + (\mathbf{1} - \tilde{\mathbf{M}}_l^{blur}) \otimes \mathbf{B}_l$ to generate the left-half image \mathbf{I}_l with smooth and natural transitions from the raindrops to the background. The similar process is conducted to generate the right-half image \mathbf{I}_r , where the corresponding right-half background image \mathbf{B}_r and DP PSF kernels \mathbf{H}_r^i are used for the same all-in-focus raindrop mask \mathbf{M}^{AiFR} . For the combined images corresponding to the images captured by a regular sensor, we generate them by averaging the left and the right images as $\mathbf{I}_c = \frac{\mathbf{I}_l + \mathbf{I}_r}{2}$ and $\mathbf{B}_c = \frac{\mathbf{B}_l + \mathbf{B}_r}{2}$.

For each real-world background DP image pair, we generate 4 different synthetic-raindrop image pairs by randomly changing the raindrop depth and mask. Each data contains the generated images of \mathbf{I}_l , \mathbf{I}_r , \mathbf{I}_c and the ground-truth background images of \mathbf{B}_l , \mathbf{B}_r , \mathbf{B}_c . We captured 613 scenes and generated 2,452 image pairs in total, among which 1,960 pairs are used for training and the rest 492 pairs are used for testing. Two samples are shown in Fig. 3(a), where noticeable DP disparities exist in the raindrop regions.

2.2 Real-World Dataset

To evaluate the generalization performance, we also collected 82 real-world DP image pairs with and without real raindrops. To minimize the impact of background refraction changes, we only used one glass panel and fixed it at a position of 15-25cm from the camera. Then, we first captured a DP image pair with the clean panel as the ground-truth images. Then, we sprayed water onto the panel to generate real raindrops and captured another DP image pair as the input images. To reduce the impact of motion, we used a solid tripod to fix the smartphone and the panel, and remotely controlled the smartphone to shoot images. As shown in Fig. 3(b), we carefully collected 82 pairs of high-quality and well-aligned DP images with and without real raindrops, containing varied and complex raindrop patterns.

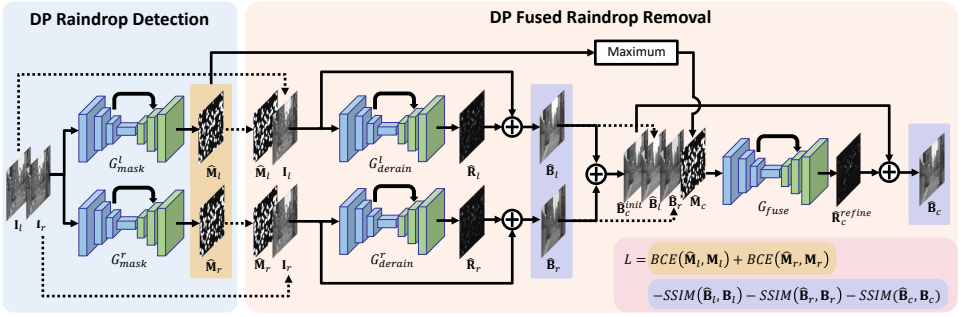


Figure 4: The overview of our proposed DP Raindrop Removal Network (DPRRN).

3 Proposed DP Raindrop Removal Network

Figure 4 shows the overview of our proposed DP Raindrop Removal Network (DPRRN). We input the pair of the left-half and the right-half images $\{I_l, I_r\}$ and estimate the clean background image \hat{B}_c as close as the ground truth B_c , where the final output \hat{B}_c is a combined image as captured by a regular sensor. Our network consists of two parts: (i) DP raindrop detection, where we conduct raindrop detection on I_l and I_r , respectively, and (ii) DP fused raindrop removal, where we remove raindrops on I_l and I_r , respectively, whose results are subsequently fused and refined for the final raindrop removal result. Each network is constructed using UNet [50] with residual blocks [42], for which we refer to the supplementary material. All the networks are trained in an end-to-end manner, as detailed below.

3.1 DP Raindrop Detection

In DP raindrop detection, the input images I_l and I_r are channel-wise concatenated and sent to two different networks G_{mask}^l and G_{mask}^r to predict two raindrop masks \hat{M}_l and \hat{M}_r , depicting the raindrop locations of I_l and I_r , respectively. For the left-half mask \hat{M}_l , the concatenated I_l and I_r are sent to G_{mask}^l to predict a pixel-wise soft raindrop mask \hat{M}_l through Sigmoid activation function at the last layer. In this process, G_{mask}^l performs raindrop localization guided with the DP disparities on the raindrops. Similarly, for the right-half mask \hat{M}_r , another network G_{mask}^r is utilized to predict a pixel-wise soft raindrop mask \hat{M}_r . Here, G_{mask}^l and G_{mask}^r are two individual networks that do not share the parameters because the disparity of I_r to I_l and the disparity of I_l to I_r show inversed shift directions and we have found using two individual networks for them achieves more robust performance.

As for the loss function on the raindrop detection, we use the Binary Cross Entropy (BCE) [42] losses as

$$L_{Mask} = BCE(\hat{M}_l, M_l) + BCE(\hat{M}_r, M_r), \quad (1)$$

where M_l and M_r are the ground-truth binary raindrop masks, where the value one means that the corresponding pixel is a part of the raindrop regions of I_l and I_r , respectively.

3.2 DP Fused Raindrop Removal

In DP fused raindrop removal, we first conduct raindrop removal of DP images I_l and I_r separately, with the guide of the estimated masks \hat{M}_l and \hat{M}_r as raindrop location clues.

For the rain removal network G_{derain}^l , we input the left-half image \mathbf{I}_l concatenated with the mask $\hat{\mathbf{M}}_l$ to derive the raindrop residuals $\hat{\mathbf{R}}_l$, from which the left-half background image is predicted as $\hat{\mathbf{B}}_l = \mathbf{I}_l - \hat{\mathbf{R}}_l$. The raindrop removal of the right-half image \mathbf{I}_r is performed in the same manner using another network G_{derain}^r to predict the right-half background image $\hat{\mathbf{B}}_r$. Here, G_{derain}^l and G_{derain}^r are also two individual networks without sharing the parameters to address the different blur kernels applied in \mathbf{I}_l and \mathbf{I}_r .

In the above processes, the background DP images $\hat{\mathbf{B}}_l$ and $\hat{\mathbf{B}}_r$ are predicted through G_{derain}^l and G_{derain}^r basically in a single image input manner. However, as the raindrop locations and the visible background information in \mathbf{I}_l and \mathbf{I}_r are slightly different according to the DP disparities, the restored background details in $\hat{\mathbf{B}}_l$ and $\hat{\mathbf{B}}_r$ are varied as well. This suggests the potential to derive a more accurate restoration result by fusing and refining the results of $\hat{\mathbf{B}}_l$ and $\hat{\mathbf{B}}_r$.

We then apply another network G_{fuse} for fusing the raindrop removal results $\hat{\mathbf{B}}_l$ and $\hat{\mathbf{B}}_r$. Because our target is to predict a clean background image as captured by a regular sensor, we calculate the corresponding mask as $\hat{\mathbf{M}}_c = \max(\hat{\mathbf{M}}_l, \hat{\mathbf{M}}_r)$ to derive a pixel-wise soft raindrop mask to the combined image \mathbf{I}_c , where \max denotes the pixel-wise maximum operation. We also calculate the initial combined background image as $\hat{\mathbf{B}}_c^{init} = \frac{\hat{\mathbf{B}}_l + \hat{\mathbf{B}}_r}{2}$. Then, the channel-wise concatenation of $\hat{\mathbf{M}}_c, \hat{\mathbf{B}}_l, \hat{\mathbf{B}}_r, \hat{\mathbf{B}}_c^{init}$ is sent to G_{fuse} to derive the residuals $\hat{\mathbf{R}}_c^{refine}$ in terms of $\hat{\mathbf{B}}_c^{init}$, from which the final output background image is derived as $\hat{\mathbf{B}}_c = \hat{\mathbf{B}}_c^{init} - \hat{\mathbf{R}}_c^{refine}$.

The DP fused raindrop removal is optimized using negative SSIM losses [29, 30] to maximize SSIMs between the raindrop removal results and the ground-truth clean background images as

$$L_{derain} = -SSIM(\hat{\mathbf{B}}_l, \mathbf{B}_l) - SSIM(\hat{\mathbf{B}}_r, \mathbf{B}_r) - SSIM(\hat{\mathbf{B}}_c, \mathbf{B}_c), \quad (2)$$

which is the simple summation of three losses for each raindrop removal output.

Combined with the DP raindrop detection and the DP fused raindrop removal, the whole DPRRN is trained using the simple summation of the mask detection loss and the raindrop removal loss as

$$L = L_{mask} + L_{derain}. \quad (3)$$

4 Experimental Results

4.1 Implementation Details

Our DPRRN is implemented using Pytorch [23] and trained on a single NVIDIA RTX3090 GPU. During the training, we use randomly cropped 480×120 patches with the batch size set to 12. To ensure that the shift directions of raindrops in the DP image pair do not change, we do not apply random flipping for data augmentation. ReLU [14] is set as the activation function. RAdam [19] is used as the optimizer to train the network with an initial learning rate of $1e^{-3}$. We adopt two-stage training, where we first train DP raindrop detection with L_{mask} only for 100 epochs without changing the learning rate and then use all the losses $L = L_{mask} + L_{derain}$ to train the whole DPRRN in end-to-end for another 400 epochs, during which the learning rate is decayed by multiplying 0.2 at 120, 240, and 360 epochs.

Table 1: Quantitative comparison on our datasets. (Red: rank 1st; Blue: rank 2nd)

Input Image Types	Methods	Synthetic		Real-World	
		PSNR	SSIM	PSNR	SSIM
Regular	AttGAN (CVPR2018) [26]	34.55	0.9614	29.59	0.9127
	CCN (CVPR2021) [27]	38.88	0.9790	27.92	0.9001
	MPRNet (CVPR2021) [39]	41.02	0.9828	30.83	0.9247
	Restormer (CVPR2022) [40]	41.94	0.9845	30.88	0.9248
	DGUNet (CVPR2022) [20]	41.32	0.9835	31.08	0.9259
Dual Pixel	RDPD+ (ICCV2021) [5]	40.51	0.9809	31.18	0.9205
	DPRRN^{-RD} (Ours)	40.93	0.9824	31.85	0.9357
	DPRRN (Ours)	42.70	0.9867	32.47	0.9396

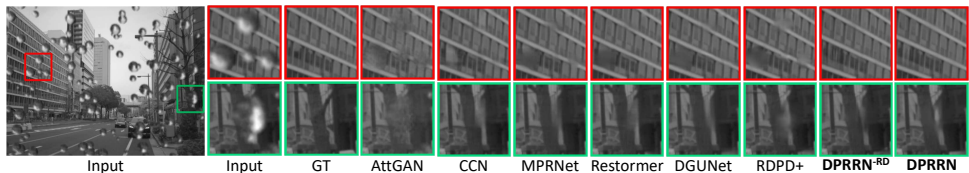


Figure 5: Qualitative comparison on the synthetic-raindrop dataset.

4.2 Comparison with State-of-the-Art Methods

Compared Methods: We compared AttGAN [26] and CCN [27], which are the methods designed for single image raindrop removal. Since AttGAN has not released the official training code, we referred to the past practice and used a third-party repository [40] to train AttGAN on our dataset. CCN is proposed to remove rain streaks and raindrops in one go. Since our current target is raindrop removal only, we took the raindrop removal part of CCN for training and comparison. We also compared general image restoration methods, MPRNet [39], DGUNet [20], and Restormer [40], which are very recent state-of-the-art methods. Although these methods are not specifically designed for raindrop removal and demonstrate their effectiveness. For all the above single image methods, the input is a regular single image, which is calculated as $\mathbf{I}_c = \frac{\mathbf{I}_l + \mathbf{I}_r}{2}$, and the output target is a clean background image in a regular sensor domain, which is supervised by the ground-truth background image calculated as $\mathbf{B}_c = \frac{\mathbf{B}_l + \mathbf{B}_r}{2}$. We used their default parameter settings to train the networks.

As a DP-based method, a recent DP-based defocus deblurring method RDPD+ [5] was compared to validate the effectiveness of our network design utilizing DP images. The input to both RDPD+ [5] and proposed DPRRN is a DP image pair \mathbf{I}_l and \mathbf{I}_r , and the final output is also supervised by a clean background image \mathbf{B}_c in a regular sensor domain. Since RDPD+ does not have specific design for defocusing deblurring, it can be directly trained on our DP synthetic-raindrop dataset. As an ablation study, we also compared our DPRRN without the DP raindrop detection part, which is denoted as DPRRN^{-RD}, where the only DP fused raindrop removal part was trained without the guide of the raindrop masks.

Results on Synthetic-Raindrop Dataset: We here show the results, where both the training and the testing were performed on the synthetic-raindrop dataset as detailed in Sec. 2.1. The second-right part of Table 1 shows the quantitative results with PSNR and SSIM. The results show that our DPRRN achieves the best performance on the synthetic data. Compared

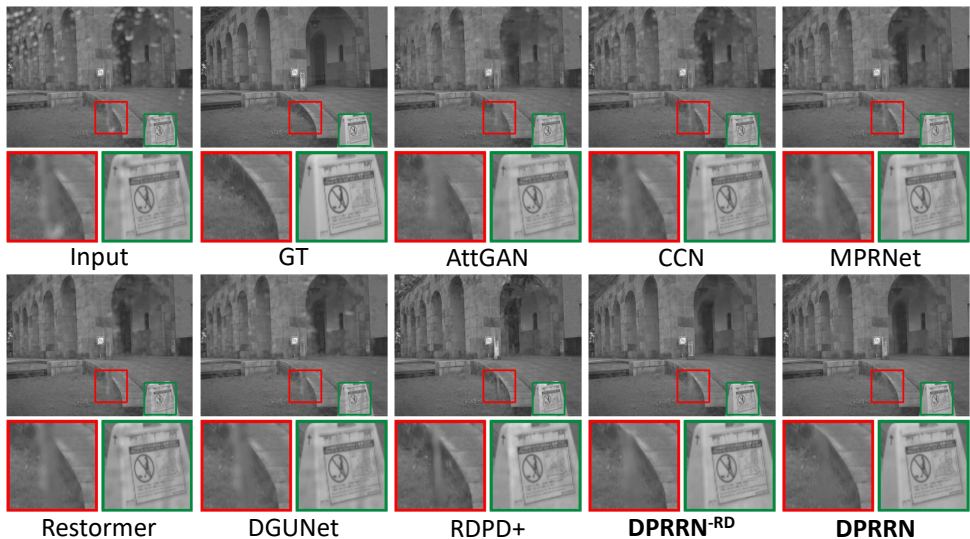


Figure 6: Qualitative comparison on the real-world dataset.

with the past single image methods, our DPRRN achieves PSNR and SSIM improvements of 0.76dB and 0.0022, respectively. Compared with the DP-based method of RDPD+, our DPRRN also achieves PSNR and SSIM improvements with the large margins of 2.19dB and 0.0043, respectively. In comparison of $\text{DPRRN}^{-\text{RD}}$ and DPRRN, we can confirm that the DP raindrop detection part significantly contributes to the performance improvement. These results validate that our DPRRN architecture can effectively exploit DP information to better remove raindrops. Figure 5 shows the qualitative results on the synthetic dataset. For the raindrops in the red box, our DPRRN can restore the thin details of window frames, while the other methods exhibit over-smoothing results. For the raindrops in the green box, our DPRRN can recover sharper details around the branches compared with the other methods.

Results on Real-World Dataset: We next show the results, where the networks were trained using the synthetic-raindrop dataset and then tested on the real-world dataset as detailed in Sec. 2.2. The rightmost part of Table 1 shows PSNR and SSIM results, demonstrating that our DPRRN exhibits large PSNR and SSIM margins of 1.29dB and 0.0137 compared with the best-performed existing methods, respectively. These margins on the real-world data are larger than those on the synthetic data (i.e., 0.76dB and 0.0022), demonstrating higher generalization ability of our DPRRN. Although MPRNet, Restormer, and DGUNet show better results than $\text{DPRRN}^{-\text{RD}}$ on the synthetic data, they show worse results than $\text{DPRRN}^{-\text{RD}}$ on the real-world dataset. This indicates that, even without the raindrop detection part, our DPRRN shows better robustness to real-world situations.

Figure 6 shows the qualitative results on the real-world dataset. The existing methods have a large number of remaining raindrops, while our DPRRN is able to remove those raindrops and restore clean and sharp background details. Especially for the red and the green box regions, our DPRRN is the only method to successfully detect and remove the long flowing raindrops, even though such a complex raindrop pattern is not included in the training data. This further validates the strong robustness of our DPRRN. More results on both the synthetic and the real-world datasets can be seen in our supplementary material.

5 Conclusion

In this paper, we have proposed the first DP-based raindrop removal network, named DPRRN, consisting of DP raindrop detection and DP fused raindrop removal. In DPRRN, we have utilized DP disparities existing in raindrop regions for robust raindrop detection and fine background detail recovery. We have also constructed both synthetic and real-world DP raindrop removal datasets to train and test our DPRRN. Using those datasets, we have experimentally demonstrated that our DPRRN outperforms existing state-of-the-art methods, showing better generalization ability to real-world raindrops. One of our future work is to jointly address rain streaks and raindrops to further boost the real-world applicability.

Acknowledgement: This work was supported by JST SPRING, Grant Number JPMJSP2106.

References

- [1] <https://github.com/MaybeShewill-CV/attentive-gan-derainnet>, 2019.
- [2] Abdullah Abuolaim and Michael S Brown. Online lens motion smoothing for video autofocus. In *Proc. of IEEE Winter Conf. on Applications of Computer Vision (WACV)*, pages 147–155, 2020.
- [3] Abdullah Abuolaim and Michael S Brown. Defocus deblurring using dual-pixel data. In *Proc. of European Conf. on Computer Vision (ECCV)*, pages 111–126, 2020.
- [4] Abdullah Abuolaim, Abhijith Punnappurath, and Michael S Brown. Revisiting autofocus for smartphone cameras. In *Proc. of European Conf. on Computer Vision (ECCV)*, pages 523–537, 2018.
- [5] Abdullah Abuolaim, Mauricio Delbracio, Damien Kelly, Michael S Brown, and Peyman Milanfar. Learning to reduce defocus blur by realistically modeling dual-pixel data. In *Proc. of IEEE Int. Conf. on Computer Vision (ICCV)*, pages 2289–2298, 2021.
- [6] Chenyi Chen, Ari Seff, Alain Kornhauser, and Jianxiong Xiao. DeepDriving: Learning affordance for direct perception in autonomous driving. In *Proc. of IEEE Int. Conf. on Computer Vision (ICCV)*, pages 2722–2730, 2015.
- [7] Yuyang Ding, Mingyue Li, Tao Yan, Fan Zhang, Yuan Liu, and Rynson WH Lau. Rain streak removal from light field images. *IEEE Trans. on Circuits and Systems for Video Technology*, 32(2):467–482, 2021.
- [8] Xueyang Fu, Jiabin Huang, Delu Zeng, Yue Huang, Xinghao Ding, and John Paisley. Removing rain from single images via a deep detail network. In *Proc. of IEEE Conf. on Computer Vision and Pattern Recognition (CVPR)*, pages 3855–3863, 2017.
- [9] Rahul Garg, Neal Wadhwa, Sameer Ansari, and Jonathan T Barron. Learning single camera depth estimation using dual-pixels. In *Proc. of IEEE Int. Conf. on Computer Vision (ICCV)*, pages 7628–7637, 2019.
- [10] Irving John Good. Rational decisions. In *Breakthroughs in statistics*, pages 365–377. Springer, 1992.

- [11] Zhixiang Hao, Shaodi You, Yu Li, Kunming Li, and Feng Lu. Learning from synthetic photorealistic raindrop for single image raindrop removal. In *Proc. of IEEE Int. Conf. on Computer Vision Workshops (CVPRW)*, pages 1–10, 2019.
- [12] Kaiming He, Xiangyu Zhang, Shaoqing Ren, and Jian Sun. Deep residual learning for image recognition. In *Proc. of IEEE Conf. on Computer Vision and Pattern Recognition (CVPR)*, pages 770–778, 2016.
- [13] Jinbeum Jang, Yoonjong Yoo, Jongheon Kim, and Joonki Paik. Sensor-based auto-focusing system using multi-scale feature extraction and phase correlation matching. *Sensors*, 15(3):5747–5762, 2015.
- [14] Alex Krizhevsky, Ilya Sutskever, and Geoffrey E Hinton. ImageNet classification with deep convolutional neural networks. In *Proc. of Advances in Neural Information Processing Systems (NIPS)*, pages 1–9, 2012.
- [15] Siyuan Li, Wenqi Ren, Feng Wang, Iago Breno Araujo, Eric K Tokuda, Roberto Hirata Junior, Roberto M. Cesar-Jr., Zhangyang Wang, and Xiaochun Cao. A comprehensive benchmark analysis of single image deraining: Current challenges and future perspectives. *Int. Journal of Computer Vision*, 129(4):1301–1322, 2021.
- [16] Xia Li, Jianlong Wu, Zhouchen Lin, Hong Liu, and Hongbin Zha. Recurrent squeeze-and-excitation context aggregation net for single image deraining. In *Proc. of European Conf. on Computer Vision (ECCV)*, pages 254–269, 2018.
- [17] Yizhou Li, Yusuke Monno, and Masatoshi Okutomi. Single image deraining network with rain embedding consistency and layered LSTM. In *Proc. of IEEE Winter Conf. on Applications of Computer Vision (WACV)*, pages 4060–4069, 2022.
- [18] Tsung-Yi Lin, Piotr Dollár, Ross Girshick, Kaiming He, Bharath Hariharan, and Serge Belongie. Feature pyramid networks for object detection. In *Proc. of IEEE Conf. on Computer Vision and Pattern Recognition (CVPR)*, pages 2117–2125, 2017.
- [19] Liyuan Liu, Haoming Jiang. Pengcheng He, Weizhu Chen, Xiaodong Liu, Jianfeng Gao, and Jiawei Han. On the variance of the adaptive learning rate and beyond. *arXiv preprint 1908.03265*, 2019.
- [20] Chong Mou, Qian Wang, and Jian Zhang. Deep generalized unfolding networks for image restoration. In *Proc. of IEEE Conf. on Computer Vision and Pattern Recognition (CVPR)*, pages 17399–17410, 2022.
- [21] Khan Muhammad, Jamil Ahmad, Zhihan Lv, Paolo Bellavista, Po Yang, and Sung Wook Baik. Efficient deep CNN-based fire detection and localization in video surveillance applications. *IEEE Trans. on Systems, Man, and Cybernetics*, 49(7):1419–1434, 2018.
- [22] Liyuan Pan, Shah Chowdhury, Richard Hartley, Miaomiao Liu, Hongguang Zhang, and Hongdong Li. Dual pixel exploration: Simultaneous depth estimation and image restoration. In *Proc. of IEEE Conf. on Computer Vision and Pattern Recognition (CVPR)*, pages 4340–4349, 2021.

- [23] Adam Paszke, Sam Gross, Francisco Massa, Adam Lerer, James Bradbury, Gregory Chanan, Trevor Killeen, Zeming Lin, Natalia Gimelshein, Luca Antiga, Alban Desmaison, Andreas Kopf, Edward Yang, Zachary DeVito, Martin Raison, Alykhan Tejani, Sasank Chilamkurthy, Benoit Steiner, Lu Fang, Junjie Bai, and Soumith Chintala. Pytorch: An imperative style, high-performance deep learning library. In *Proc. of Advances in Neural Information Processing Systems (NeurIPS)*, pages 8026–8037, 2019.
- [24] Abhijith Punnappurath and Michael S Brown. Reflection removal using a dual-pixel sensor. In *Proc. of IEEE Conf. on Computer Vision and Pattern Recognition (CVPR)*, pages 1556–1565, 2019.
- [25] Abhijith Punnappurath, Abdullah Abuolaim, Mahmoud Afifi, and Michael S Brown. Modeling defocus-disparity in dual-pixel sensors. In *Proc. of IEEE Int. Conf. on Computational Photography (ICCP)*, pages 1–12, 2020.
- [26] Rui Qian, Robby T Tan, Wenhan Yang, Jiajun Su, and Jiaying Liu. Attentive generative adversarial network for raindrop removal from a single image. In *Proc. of IEEE Conf. on Computer Vision and Pattern Recognition (CVPR)*, pages 2482–2491, 2018.
- [27] Ruijie Quan, Xin Yu, Yuanzhi Liang, and Yi Yang. Removing raindrops and rain streaks in one go. In *Proc. of IEEE Conf. on Computer Vision and Pattern Recognition (CVPR)*, pages 9147–9156, 2021.
- [28] Yuhui Quan, Shijie Deng, Yixin Chen, and Hui Ji. Deep learning for seeing through window with raindrops. In *Proc. of IEEE Int. Conf. on Computer Vision (ICCV)*, pages 2463–2471, 2019.
- [29] Dongwei Ren, Wangmeng Zuo, Qinghua Hu, Pengfei Zhu, and Deyu Meng. Progressive image deraining networks: A better and simpler baseline. In *Proc. of IEEE Conf. on Computer Vision and Pattern Recognition (CVPR)*, pages 3937–3946, 2019.
- [30] Dongwei Ren, Wei Shang, Pengfei Zhu, Qinghua Hu, Deyu Meng, and Wangmeng Zuo. Single image deraining using bilateral recurrent network. *IEEE Trans. on Image Processing*, 29:6852–6863, 2020.
- [31] Olaf Ronneberger, Philipp Fischer, and Thomas Brox. U-net: Convolutional networks for biomedical image segmentation. In *Proc. of Int. Conf. on Medical Image Computing and Computer-Assisted Intervention (MICCAI)*, pages 234–241, 2015.
- [32] Ming-Wen Shao, Le Li, De-Yu Meng, and Wang-Meng Zuo. Uncertainty guided multi-scale attention network for raindrop removal from a single image. *IEEE Trans. on Image Processing*, 30:4828–4839, 2021.
- [33] Mingwen Shao, Le Li, Hong Wang, and Deyu Meng. Selective generative adversarial network for raindrop removal from a single image. *Neurocomputing*, 426:265–273, 2021.
- [34] Hong Wang, Qi Xie, Qian Zhao, and Deyu Meng. A model-driven deep neural network for single image rain removal. In *Proc. of IEEE Int. Conf. on Computer Vision (CVPR)*, pages 3103–3112, 2020.

- [35] Tianyu Wang, Xin Yang, Ke Xu, Shaozhe Chen, Qiang Zhang, and Rynson WH Lau. Spatial attentive single-image deraining with a high quality real rain dataset. In *Proc. of IEEE Int. Conf. on Computer Vision (CVPR)*, pages 12270–12279, 2019.
- [36] Shumian Xin, Neal Wadhwa, Tianfan Xue, Jonathan T Barron, Pratul P Srinivasan, Jiawen Chen, Ioannis Gkioulekas, and Rahul Garg. Defocus map estimation and deblurring from a single dual-pixel image. In *Proc. of IEEE Int. Conf. on Computer Vision (CVPR)*, pages 2228–2238, 2021.
- [37] Tao Yang, Xiaofei Chang, Hang Su, Nathan Crombez, Yassine Ruichek, Tomas Krajinik, and Zhi Yan. Raindrop removal with light field image using image inpainting. *IEEE Access*, 8:58416–58426, 2020.
- [38] Wenhan Yang, Robby T Tan, Jiashi Feng, Jiaying Liu, Zongming Guo, and Shuicheng Yan. Deep joint rain detection and removal from a single image. In *Proc. of IEEE Conf. on Computer Vision and Pattern Recognition (CVPR)*, pages 1357–1366, 2017.
- [39] Syed Waqas Zamir, Aditya Arora, Salman Khan, Munawar Hayat, Fahad Shahbaz Khan, Ming-Hsuan Yang, and Ling Shao. Multi-stage progressive image restoration. In *Proc. of IEEE Conf. on Computer Vision and Pattern Recognition (CVPR)*, pages 14821–14831, 2021.
- [40] Syed Waqas Zamir, Aditya Arora, Salman Khan, Munawar Hayat, Fahad Shahbaz Khan, and Ming-Hsuan Yang. Restormer: Efficient transformer for high-resolution image restoration. In *Proc. of IEEE Conf. on Computer Vision and Pattern Recognition (CVPR)*, pages 5728–5739, 2022.
- [41] Kaihao Zhang, Wenhan Luo, Yanjiang Yu, Wenqi Ren, Fang Zhao, Changsheng Li, Lin Ma, Wei Liu, and Hongdong Li. Beyond monocular deraining: Parallel stereo deraining network via semantic prior. *Int. Journal of Computer Vision*, pages 1–16, 2022.
- [42] Yinda Zhang, Neal Wadhwa, Sergio Orts-Escolano, Christian Häne, Sean Fanello, and Rahul Garg. Du2net: Learning depth estimation from dual-cameras and dual-pixels. In *Proc. of European Conf. on Computer Vision (ECCV)*, pages 582–598, 2020.
- [43] Simone Zini and Marco Buzzelli. Laplacian encoder-decoder network for raindrop removal. *Pattern Recognition Letters*, 158:24–33, 2022.